Check for updates

Melting of hybrid organic–inorganic perovskites

Bikash Kumar Shaw [1], Ashlea R. Hughes [2], Maxime Ducamp [3], Stephen Moss[2], Anup Debnath [4], Adam F. Sapnik [1], Michael F. Thorne[1], Lauren N. McHugh [1], Andrea Pugliese [2], Dean S. Keeble[5], Philip Chater [5], Juan M. Bermudez-Garcia [1,6], Xavier Moya[1], Shyamal K. Saha[4], David A. Keen [7], François-Xavier Coudert [3], Frédéric Blanc [2,8] and Thomas D. Bennett [1✉]

Several organic–inorganic hybrid materials from the metal–organic framework (MOF) family have been shown to form stable liquids at high temperatures. Quenching then results in the formation of melt-quenched MOF glasses that retain the three-dimensional coordination bonding of the crystalline phase. These hybrid glasses have intriguing properties and could find practical applications, yet the melt-quench phenomenon has so far remained limited to a few MOF structures. Here we turn to hybrid organic–inorganic perovskites—which occupy a prominent position within materials chemistry owing to their functional properties such as ion transport, photoconductivity, ferroelectricity and multiferroicity—and show that a series of dicyanamide-based hybrid organic–inorganic perovskites undergo melting. Our combined experimental–computational approach demonstrates that, on quenching, they form glasses that largely retain their solid-state inorganic–organic connectivity. The resulting materials show very low thermal conductivities (~0.2 W m⁻¹ K⁻¹), moderate electrical conductivities (10⁻³–10⁻⁵ S m⁻¹) and polymer-like thermomechanical properties.

Hybrid organic–inorganic perovskites (HOIPs) are a family of materials with the structure ABX$_3$ where A is an organic cation, B is a metal ion and X is a bridging ligand. They occupy a prominent position within solid state chemistry and materials science due to interest in their utility in, for example, ionic transport, ferroelectric, luminescent and multiferroic applications[1–3]. In particular, hybrid lead halide perovskites have been extensively studied for their performance and efficiency in photovoltaic devices[4,5]. The replacement of the halide ion by flexible bidentate bridging ligands, such as formate (HCOO⁻)[6], hypophosphite (H$_2$POO⁻)[7] and dicyanamide (dca, N(CN)$_2$⁻)[8], gives rise to an even wider array of functional properties while preserving their three-dimensional coordination polymer structures[9].

Crystalline materials dominate the field of HOIP research and show rich structural behaviour such as octahedral tilting, columnar shifts and molecular disordering associated with phase transitions[10]. Non-crystalline materials receive comparatively little attention, although the reversible pressure-induced amorphization of three dimensional methylammonium lead halide perovskites has been studied[11,12] alongside melting of the two-dimensional layered HOIP series [(C$_4$H$_9$NH$_3$)$_2$MI$_4$] (M = Ge, Sn, Pb)[13].

Solid–liquid transitions have started to be reported in the related family of three-dimensional metal–organic frameworks (MOFs). For example, the melt-quenching of several Zn(C$_3$H$_3$N$_2$)$_2$ structures results in the formation of a new category of glasses which are structurally similar to silica glass yet contain linked inorganic and organic components[14]. Routes to expand hybrid glasses are highly sought after, although the limited chemical variance within both glass-forming MOFs and lower dimensionality coordination polymers means only a relatively small number have been reported.

Motivated by the great chemical variability across the dense ABX$_3$ perovskite family, in this Article we extend the phenomena of

melting and melt-quenching in HOIPs. Three [TPrA][M(dca)$_3$] (TPrA = tetrapropylammonium (CH$_3$CH$_2$CH$_2$)$_4$N⁺, M = Mn²⁺, Fe²⁺, Co²⁺) materials were selected for study due to the multiple coordination modes possible for the dca ligands. These bridge transition metal cations through the N atom in μ$_{1,5}$ end-to-end connectivity (Fig. 1a). At room temperature, both [TPrA][Co(dca)$_3$] and [TPrA][Fe(dca)$_3$] crystallize in the orthorhombic space group (Pnna) as opposed to the tetragonal Mn analogue which crystallizes in P$\bar{4}$2$_1$c (refs. [8,15]).

In this Article, we show that these materials melt at temperatures lower than existing MOFs and comply with the Lindemann criteria for melting. We also investigate decoordination and decomposition processes in the family. Recrystallization observed in lower dimensional zinc phosphate coordination polymer glasses may be avoided[16], whilst the presence of organic cations distinguishes them from the three-dimensional MOFs found to melt thus far. We also show that the glassy products demonstrate potentially useful thermal and electrical conductivities.

Results

Glass formation and thermal properties. Single crystals of [TPrA][M(dca)$_3$] (M = Mn²⁺, Fe²⁺, Co²⁺) were obtained by solvent layering, following previously reported procedures (Methods, Supplementary Fig. 1)[8,15]. Thermogravimetric analysis (TGA) gave decomposition temperatures (T_ds) of 281, 273 and 267 °C for the Mn, Fe and Co analogues, respectively (Supplementary Fig. 2), in agreement with the literature[17]. Differential scanning calorimetry (DSC) was carried out on each sample and sharp endotherms were identified at temperatures far in excess of the reported solid–solid polymorphic phase transitions[8,15]. These correspond to unreported melting temperatures (T_ms) of 271, 263 and 230 °C for the Mn, Fe and Co analogues, respectively (Fig. 1b). Weight losses at T_m were less than

[1]Department of Materials Science and Metallurgy, University of Cambridge, Cambridge, UK. [2]Department of Chemistry, University of Liverpool, Liverpool, UK. [3]Chimie ParisTech, PSL University, CNRS, Institut de Recherche de Chimie Paris, Paris, France. [4]School of Materials Sciences, Indian Association for the Cultivation of Science, Jadavpur, India. [5]Diamond Light Source Ltd, Diamond House, Harwell Campus, Didcot, UK. [6]University of A Coruna, QuiMolMat Group, Department of Chemistry, Faculty of Science and Advanced Scientific Research Center (CICA), Zapateira, Spain. [7]ISIS Facility, Rutherford Appleton Laboratory, Harwell Campus, Didcot, UK. [8]Stephenson Institute for Renewable Energy, University of Liverpool, Liverpool, UK. ✉e-mail: tdb35@cam.ac.uk
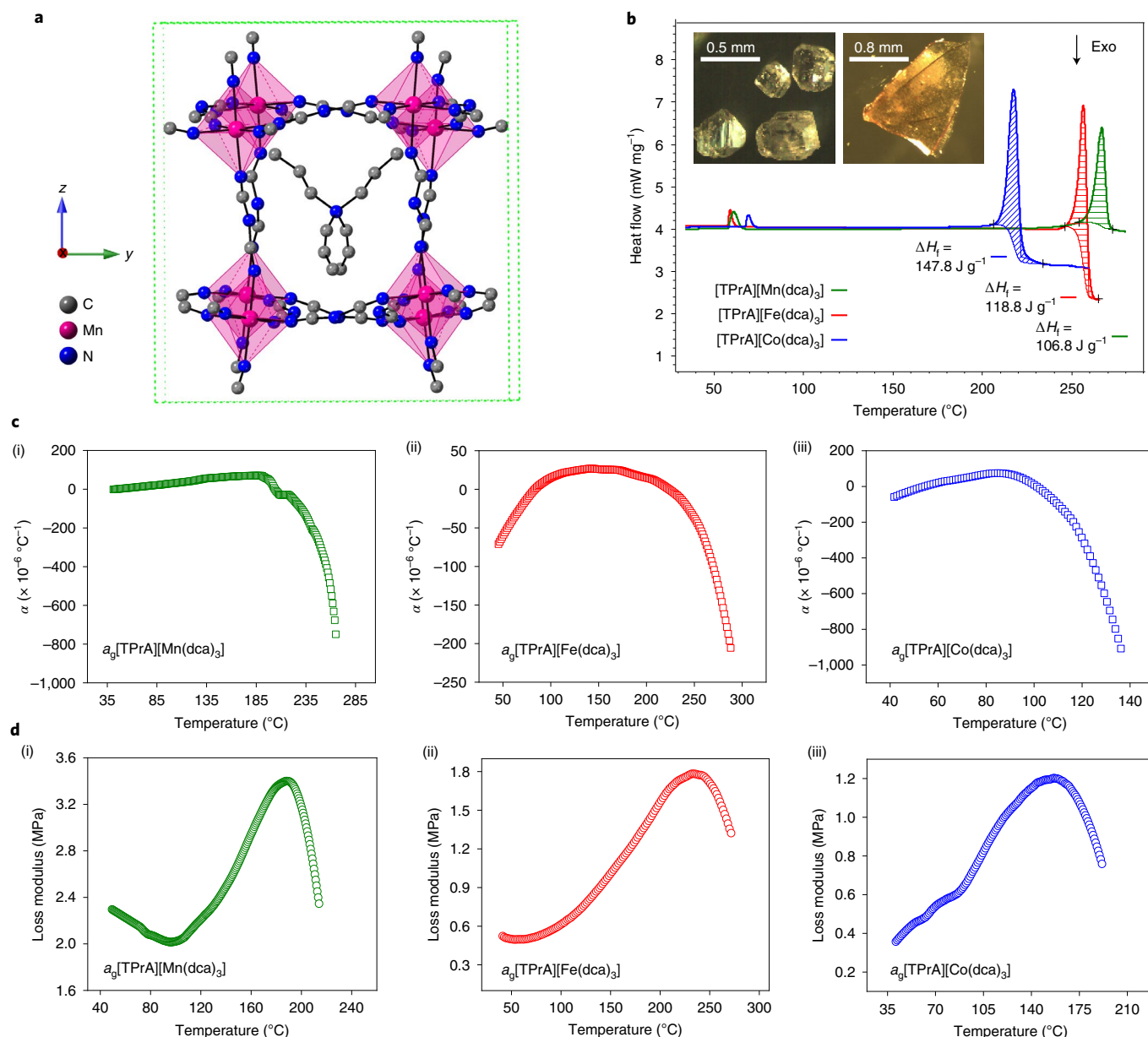
Fig. 1 | Glass formation from hybrid perovskites. a, Simplified representation of the [TPrA][Mn(dca)$_3$] structure at room temperature. Atom colour code: Mn, pink; C, grey; N, blue. All H atoms have been omitted for clarity, as have all TPrA ions except that located on the body-centre position. Furthermore, only one of the possible orientations of the TPrA and dca ions within the average crystal structure is shown[8]. Green dashed lines indicate the unit cell. **b**, Change in heat flow with increase in temperature for [TPrA][M(dca)$_3$] samples (M = Mn^{2+}, Fe^{2+}, Co^{2+}). Values for the enthalpy of fusion (ΔH_f) for the crystalline-to-liquid transition were extracted from the shaded sigmoidal areas, which were determined after subtracting sigmoidal baselines from the calorimetric data. Inset: optical images of [TPrA][Mn(dca)$_3$] before heating (left) and after cooling (right). **c**, Variations of the average coefficient of linear thermal expansion (α) are shown with temperature for the glasses (a_g[TPrA][M(dca)$_3$]) for M = Mn^{2+} (i), Fe^{2+} (ii) and Co^{2+} (iii). Sudden drops in α indicate the T_f point in each case (Supplementary Fig. 9). **d**, Variation of the loss modulus as a function of temperature for a_g[TPrA][M(dca)$_3$] for M = Mn^{2+} (i), Fe^{2+} (ii) and Co^{2+} (iii), obtained from dynamic mechanical analysis at 1 Hz. Glass transition temperatures (T_gs) were determined from peak values and are given in Table 1.

0.5% in all cases. The increase in melting temperature from Co to Mn follows the trend in the ionic radii $r_{Co} < r_{Fe} < r_{Mn}$. This is consistent with hard–soft/acid–base theory in which softer metal centres like Mn^{2+} may interact more favourably with the softer dca ligand.

Crystalline samples of [TPrA][M(dca)$_3$] (M = Mn^{2+}, Fe^{2+}, Co^{2+}) were heated in a simultaneous DSC–TGA experiment to temperatures above T_m, before cooling back to room temperature (Methods). Partial recrystallization of a_g[TPrA][Mn(dca)$_3$] and a_g[TPrA]

[Fe(dca)$_3$] occurred on cooling from lower temperatures. The glasses, in keeping with existing nomenclature on hybrid glasses, are termed a_g[TPrA][M(dca)$_3$] (a_g: melt-quenched glass). Liquid-like behaviour was evident from the physical appearance of the samples on cooling from 277 °C (Mn), 269 °C (Fe) and 264 °C (Co) and their amorphous X-ray diffraction patterns (Supplementary Figs. 3–6). Subsequent DSC experiments (Methods) yielded smooth but very weak changes in the heat flow, indicative of glass transition temperatures (T_gs) at 218, 225 and 125 °C for a_g[TPrA][Mn(dca)$_3$],

Table 1 | Physical properties of solid–liquid transitions in hybrid perovskites

Sample	T_m (°C)	ΔH_{fus} (J g⁻¹)	T_g, DSC (°C)	TMA (°C)	DMA, onset of storage modulus (°C)	DMA, peak of loss modulus (°C)	E_a (kJ mol⁻¹)
[TPrA][Mn(dca)₃]	271	106.8	218	209	183	185	49.9
[TPrA][Fe(dca)₃]	263	118.8	225	220	213	219	28.2
[TPrA][Co(dca)₃]	230	147.8	125	102	146	145	47.1

Errors associated with determination of T_g are typically up to 2 °C from DSC and 10–20 °C from DMA (ref. [49]).

a_g[TPrA][Fe(dca)₃] and a_g[TPrA][Co(dca)₃], respectively (Table 1, Supplementary Fig. 7). Like zeolitic imidazolate framework (ZIF) glasses (T_g/T_m ~0.9), a deviation from the empirical 'T_g/T_m ~2/3' law is observed, ($|2/3 - T_g/T_m| = (0.14–0.18)$)[18]. Small weight losses of <0.5% for the Mn, Fe and Co glasses on heating to their respective T_gs were noted (Supplementary Fig. 8).

Thermomechanical analysis (TMA) was performed on the a_g[TPrA][M(dca)₃] samples and the resultant dilatometric softening temperatures (T_fs), that is where the solid glass began to transform into a softer state, were used to corroborate the values of T_g extracted from DSC measurements (Fig. 1c, Supplementary Fig. 9). Frequency-dependent dynamic mechanical analysis (DMA), a more sensitive method of obtaining the glass transition temperature, was performed and T_g values of 185, 219 and 145 °C for a_g[TPrA][Mn(dca)₃], a_g[TPrA][Fe(dca)₃] and a_g[TPrA][Co(dca)₃] were identified, using the maximum value of the loss modulus (Fig. 1d, Supplementary Fig. 10)[16]. These agree well with those obtained from TMA and DSC measurements (Table 1).

The shift in T_g to higher temperature with increasing applied frequency was used to calculate activation energies (E_a) associated with T_g using the Arrhenius equation (equation (1), Table 1, Supplementary Fig. 11, Supplementary Table 1).

$$\ln\frac{f_1}{f_2} = \frac{E_a}{R}\left(\frac{1}{T_{g_2}} - \frac{1}{T_{g_1}}\right) \tag{1}$$

where f_1, f_2 are the applied frequencies, T_{g_1}, T_{g_2} are glass transition temperatures at the applied frequencies and R is the ideal gas constant.

Delineating decoordination and decomposition. ^{13}C magic angle spinning (MAS) NMR spectra of [TPrA][Mn(dca)₃], [TPrA][Fe(dca)₃] and [TPrA][Co(dca)₃] before and after melt-quenching were obtained (Fig. 2, Supplementary Figs. 12–14) under optimized conditions for paramagnetic systems[19–21]. Spectra of [TPrA][Fe(dca)₃] and [TPrA][Co(dca)₃] contain one resonance per type of carbon in the TPrA cation in the 200 to –100 ppm region and two (or more) poorly resolved resonances around 3,900 ppm for the NCN carbon of the dca anions (see below and Supplementary Figs. 15 and 16 for spectral assignment). By contrast, in crystalline [TPrA][Mn(dca)₃] where the NMR lines are much narrower, resonances for each type of carbon in the TPrA and dca ions (for example the NCN resonances appear as two resolved shifts of 7 and 3 ppm in a 2:1 ratio) can be observed (Supplementary Fig. 17). These observations are consistent with the phases expected based on previous reports of phase transitions in the family (Methods)[15]. The spectra were assigned based on known chemical shift values for TPrA in diamagnetic systems[22], spatial proximity to the metal centres and ^{13}C-edited experiments using ^{1}H-^{13}C transferred echo double resonance (TEDOR)[21,23] that filter out any non-protonated carbons (Supplementary Figs. 12–14). The absence of a ^{13}C signal at ~3,900 ppm in both [TPrA][Fe(dca)₃] and [TPrA][Co(dca)₃] TEDOR spectra strongly supports its assignment to the NCN carbon of the dca anions, which contain the only quaternary carbon

amongst both TPrA and dca ions. Therefore, it is postulated that the very large paramagnetic shifts observed in dca result from its μ$_{1,5}$ bonding mode to two metal centres (Fig. 1a). Notably, the NCN carbon within the [TPrA][Fe(dca)₃] and [TPrA][Co(dca)₃] materials appears at a very similar chemical shift, which is also seen elsewhere in the literature[24]. The ^{13}C shifts of the TPrA cation are significantly less affected due to the greater distance of this A site cation from the metal centres (Fig. 1a), whilst the different chemical shift of the dca ligand in crystalline [TPrA][Mn(dca)₃] (~5 ppm, Fig. 2, Supplementary Fig. 12 and Supplementary Table 2) is ascribed to the difference in magnetic susceptibility of Mn^{2+}, in comparison to Fe^{2+} and Co^{2+}. This yields smaller anisotropic bulk magnetic susceptibility broadening in the former, consistent with ^{7}Li MAS NMR of LiMPO₄ (M = Mn^{2+}, Fe^{2+}, Co^{2+})[19,24].

Comparison of the spectra of crystalline and glass samples (Fig. 2, Supplementary Figs. 12–14) shows similar chemical shifts in the TPrA region, suggesting that the 'A' site cation remains intact during the melt-quenching process. No resonances for the dca carbons are observed in their paramagnetic NMR regions for any of the quenched glasses. This is due to a likely decrease in the transverse magnetization decay time constant with refocused inhomogeneous broadening T_2' and an increase in line broadening on vitrification and hence an increase in paramagnetic broadening of the glasses.

Experimental evidence for the decoordination of dca ligands during the melting process arises from an additional resonance at 120 ppm in the spectra for a_g[TPrA][Fe(dca)₃], which is assigned to a 'free' dca ligand[25]. A further peak at 159 ppm, combined with the appearance of two (weak) absorption bands at 1,629–1,634 cm⁻¹ and 802–806 cm⁻¹ in the infrared spectra for all glasses, also indicates a degree of ligand decomposition on melting (Supplementary Fig. 18)[17,25,26].

Liquid phase ^{1}H and ^{13}C NMR spectra (Supplementary Figs. 19–24) and high-resolution mass spectrometry (HRMS) data (Supplementary Figs. 25–30) of 'digested' samples were collected. The ^{1}H and ^{13}C spectra for crystalline [TPrA][Co(dca)₃] each contain the expected three resonances of [TPrA] while NMR signals for an H₂O-protonated dca ligand, that is known to exist as an aminonitrile–carbodiimide tautomer as for all cyanamides (Supplementary Scheme 1), are observed and further detected in the HRMS data. Specifically, in the NMR data (Supplementary Figs. 23 and 24), the resulting NH appears at 7.5 ppm in the ^{1}H NMR spectrum. We ascribe the 153 and 110 ppm signals in the ^{13}C NMR spectrum to the NH=C=N carbodiimide and C≡N nitrile carbons of the dca ligand, respectively[27], whilst the HRMS data (Supplementary Figs. 29 and 30) show both [TPrA] and dca ligands. The similar corresponding NMR and HRMS spectra for a_g[TPrA][Co(dca)₃] indirectly confirm the presence of both dca and TPrA ligands. Similar NMR results were obtained for the Mn and Fe samples (Supplementary Figs. 19–22 and 25–28), although hyperfine coupling in the NMR spectra induced poor signal-to-noise ratios and spectral broadening that render detection of some of the dca carbons more challenging.

Further evidence for the partial decoordination of dca ligands is provided by diffuse reflectance UV-Vis spectroscopy measurements (Supplementary Fig. 31). Specifically, the spectrum for a_g[TPrA]
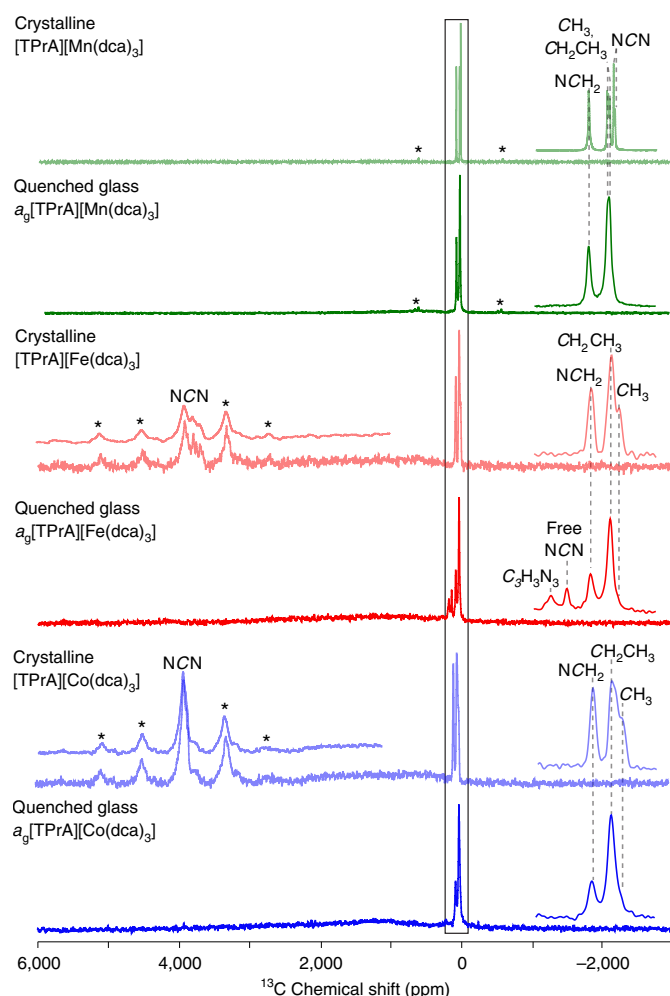
Fig. 2 | Structural insights into melting and glass structure. [13]C double adiabatic echo MAS NMR spectra of crystalline [TPrA][Mn(dca)$_3$] before heating (pale green), after melt-quenching (green), crystalline [TPrA][Fe(dca)$_3$] (pale red), after melt-quenching (red), crystalline [TPrA][Co(dca)$_3$] before heating (pale blue) and after melt-quenching (blue). Magnified views of the 200 to −100 ppm region (within the box) are shown on the right hand side with spectral assignments. Spectra were processed with exponential line broadenings (of 20 Hz), appropriate for the magnified views shown in order to capture the various spectral features, while the overlaid views in the 6,000 to 1,000 ppm paramagnetic shifts region show data processed with increased line broadenings (of 200 Hz) taking into account the larger linewidths of the NCN resonances of the dca ligand. C$_3$H$_3$N$_3$ corresponds to triazine-based structures. Asterisks (*) denote spinning sidebands.

[Co(dca)$_3$] contains only two electronic absorption bands. This is in contrast to the three that would be expected for d^7 tetrahedral Co(II), belonging to the $^4A_2 \rightarrow {}^4T_2$, $^4A_2 \rightarrow {}^4T_1(F)$ and $^4A_2 \rightarrow {}^4T_1(P)$[28] electronic transitions and consistent with the blue colour (Supplementary Fig. 32)[29].

Temperature dependent d.c. magnetic susceptibility measurements were carried out and the variation of $\chi_M T$ (χ_M: molar magnetic susceptibility) as a function of T indicated antiferromagnetic coupling for all samples at low temperatures (Supplementary Figs. 33 and 34)[30]. Room temperature $\chi_M T$ values for the glasses were smaller than those for the crystalline phases, indicating a reduction in oxidation state for a proportion of metal centres. These differences were used to calculate the percentage of metal ions reduced to M(0) on melt-quenching in each case (a_g[TPrA][Mn(dca)$_3$] 18.7%,

a_g[TPrA][Fe(dca)$_3$] 22.0% and a_g[TPrA][Co(dca)$_3$] 15.3%), which agree well with those calculated by comparison of X-ray photoelectron spectroscopy (XPS) spectra (Supplementary Figs. 35–39, Supplementary Table 3).

Atomistic insight into melting. Room-temperature total scattering data for [TPrA][M(dca)$_3$] show Bragg peaks arising from long-range order (Supplementary Fig. 40). By contrast, the data for the corresponding glasses, a_g[TPrA][M(dca)$_3$] show smooth broad humps without any major Bragg peaks (Supplementary Fig. 41). The X-ray pair distribution functions (PDFs), $D(r)$, were extracted after appropriate data corrections (Fig. 3a,b and Supplementary Figs. 42 and 43). To aid assignment of the peaks in the PDFs, the published structures for the crystalline samples were refined using the PDF data and weighted partial pair distributions, $g_{ij}(r)$, were calculated (Supplementary Methods, Supplementary Figs. 44–49).

Peaks in the $D(r)$ for the crystalline samples at $r = \sim 1.3$ Å contain contributions from both from C–C and C–N (including C≡N) atom pairs, whilst the peak at $r = 2.05$–2.25 Å is ascribed predominantly to the M–N correlation (Fig. 3a, Supplementary Figs. 42 and 43). The movement of this peak to lower r, from Mn–N to Fe–N and to Co–N agrees well with the experimentally reported M–N distances. The strongest contribution to the peak at $r = \sim 8.2$ Å is primarily from the M–M distance in each case.

As expected, high r peaks broaden and weaken on melt-quenching in each case (Fig. 3b, Supplementary Figs. 42 and 43). Nevertheless, the (now broad) peak centred around $r = \sim 8.2$ Å is the highest-r feature in $D(r)$ for each glass and would therefore be consistent with the retention of some M–dca–M linkages. The broadening of peaks below 2 Å may arise as the result of partial decomposition. Decoordination of dca linkers is also shown. For example, the peak at 3.3 Å, which mainly arises from the M–N–C correlation, appears to split into two peaks in the glass in each case. A partial splitting/broadening is also observed in the peak at 4.7 Å, which contains overlapping contributions from the M–N, M–C and C–C correlations.

First-principles molecular dynamics (FPMD) simulations were then employed in order to characterize the microscopic evolution of [TPrA][Mn(dca)$_3$] on melting (Fig. 3c–e). The dynamic nature of bond breaking prevented the use of classical force fields and so FPMD simulations based on a quantum chemical description of the system at the density functional theory level were chosen (Methods). Four separate molecular dynamics simulations were performed on the crystalline material, at 300, 750, 1,200 and 1,700 K. Structural, dynamical and thermodynamic properties were analysed along each trajectory. We note that most of these temperatures are far above the experimental ones as simulations describing bond-breaking close to T_m would require simulations on the (impractical) microsecond timescale.

The PDFs at each temperature were calculated and show the expected significant thermal broadening for Mn–N distances, in addition to the loss of long-range order ($r > 6$ Å) at the higher temperatures (Fig. 3c). The generalized Lindemann ratio was calculated for the Mn–N peak width and it was found to exceed the Lindemann ratio for melting (10% to 15%) between 750 and 1,200 K (Supplementary Table 4)[31]. Analysis of the N–Mn–N angles also confirms increased thermal fluctuations of the perfect octahedral environment on heating (Supplementary Fig. 50), with broadening of the N–Mn–N bond angle peak centred at 90°. Analysis of the mean square displacement of [TPrA][Mn(dca)$_3$] over time (Fig. 3e) confirmed the liquid-like nature of the resulting melt, with a transition from restricted motion (less than 1 Å²) resulting from framework vibrations at 300 K to diffusive behaviour at 750 K and higher temperatures.

Observation of the trajectories showed breaking and re-formation of Mn–N bonds in the liquid state, in addition to
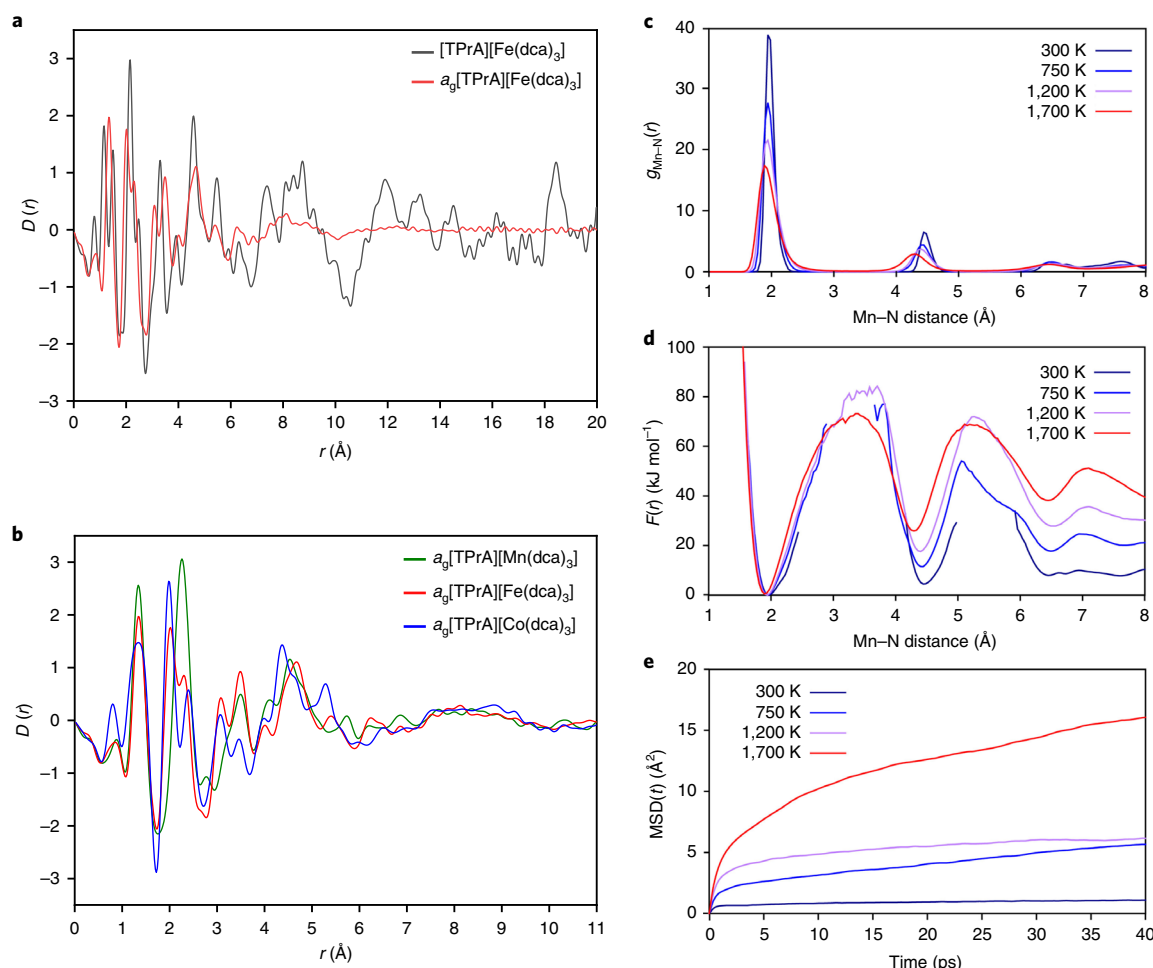
Fig. 3 | Pair distribution function analysis. a, PDFs of [TPrA][Fe(dca)$_3$] and the corresponding glass a_g[TPrA][Fe(dca)$_3$]. **b**, PDFs of a_g[TPrA][Fe(dca)$_3$], a_g[TPrA][Co(dca)$_3$] and a_g[TPrA][Mn(dca)$_3$]. **c**, Evolution of the partial radial distribution function $g_{ij}(r)$ for Mn–N distances in [TPrA][Mn(dca)$_3$] at temperatures from 300 K (navy blue) to 1,700 K (red), from first principles molecular dynamics (FPMD). **d**, Potential of mean force $F(r)$ along the Mn–N distance coordinate at different temperatures. The discontinuities of some of the data arise from $F(r)$ being ill-defined for null values of $g_{Mn-N}(r)$. Data from FPMD. **e**, Mean square displacement as a function of time (MSD(t)) for [TPrA][Mn(dca)$_3$], for temperatures ranging from 300 K (navy blue) to 1,700 K (red). Data from FPMD.

significant movement of the propyl groups of the TPrA cations, starting at 1,200 K. A series of free energy profiles from the Mn–N PDFs was therefore calculated (Fig. 3d). These potentials of mean force, that is $F(r) = -kT \ln g(r)$, are expressed as a function of the Mn–N distance and show that the mechanism of melting is similar to that previously established in the ZIF family. This is confirmed by the reduction in the number of six-coordinated Mn atoms on Mn–N bond breaking that is analogous to coordination reduction observed in melting in ZIFs (Supplementary Fig. 51)[14].

From these data, we were able to fit the concentration, n_d, of five-coordinated M^{2+} ions, considered as a 'defect' in the structure, with $n_d \propto \exp(-\Delta_f H_d / RT)$ and estimate an enthalpy for formation of $\Delta_f H_d$ ~91 kJ mol^{-1} (estimated between 1,200 and 1,700 K). The value of the free energy barrier to melting (Fig. 3d) was estimated as ~85 kJ mol^{-1} at 1,200 K, similar to other framework materials[14]. This significant barrier confirms that, as in conventional solids, melting occurs through a rare barrier-crossing event. However, in contrast with the case of porous MOFs, where this barrier is strongly temperature dependent, here the impact of temperature is smaller, meaning that the activation entropy involved is lower. We link this to the higher metal node coordination number of the materials considered here compared to those of ZIFs.

Electrical and thermal conductivity. Frequency-dependent electrical conductivity measurements were carried out to probe the charge-transport behaviour of the a_g[TPrA][M(dca)$_3$] samples and values of the in-phase a.c. impedance (Z') were plotted with the corresponding out-of-phase component (Z'') (Fig. 4a–c). Values of d.c. resistance were evaluated after fitting of the semicircular Nyquist plot. We ascribe the low-frequency dispersion as the result of electrode polarization occurring when the material is subjected to an oscillating electric field[32]. Room temperature d.c conductivities (σ_{RT}) of 0.02 × 10^{-4}, 2.5 × 10^{-3} and 0.66 × 10^{-4} S m^{-1} for the Mn-, Fe- and Co-based glasses characterize these as moderately-conducting materials (Table 2). However, all conductivities are orders of magnitude larger than for the corresponding crystalline frameworks (0.09 × 10^{-5}, 0.64 × 10^{-5} and 0.09 × 10^{-5} S m^{-1}, respectively, Supplementary Fig. 52). Therefore, we postulate inter- or intra-chain hopping involving the delocalized electron pair of the dca linker. Such a mechanism would be consistent with the increase in conductivity for the glasses, where the dca linker movement may be less constrained[33].

The thermal conductivity of glasses is also of great importance given the applications of inorganics in, for example, thermoelectric materials[34] for waste-heat power generation and solid-state Peltier coolers[35]. The heat conductivity of the a_g[TPrA][M(dca)$_3$] series was probed,
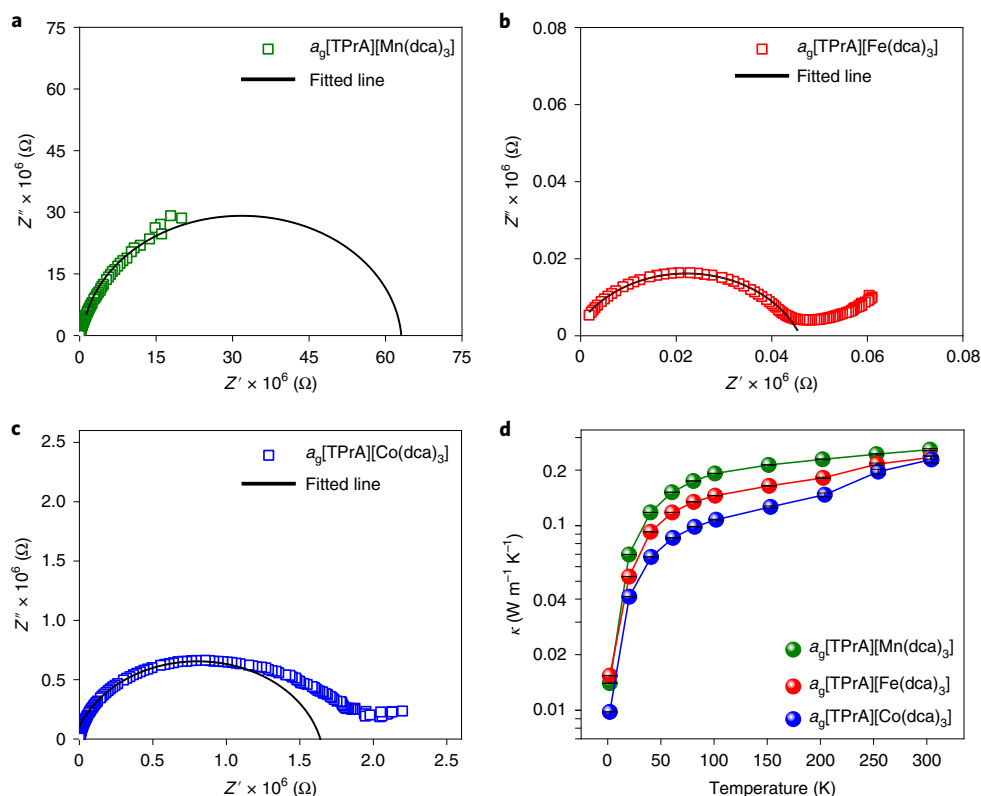
Fig. 4 | Physical properties of melt-quenched glasses. a–c, Nyquist plot of real (Z') and imaginary (Z'') parts of impedance values for a_g[TPrA][Mn(dca)$_3$] (**a**), a_g[TPrA][Fe(dca)$_3$] (**b**) and a_g[TPrA][Co(dca)$_3$] (**c**) at 300 K. The cut-off point of the fitted theoretical line (black) at the x axis gives the value of the d.c. resistance. Low-frequency (that is data points furthest from the origin) dispersion occurs due to electrode polarization. **d**, Logarithmic variation of thermal conductivity (κ) as a function of temperature for a_g[TPrA][M(dca)$_3$] from 2 to 300 K.

Table 2 | Physical properties of melt-quenched glasses

Sample	E (GPa)	ρ_c (g cm^{-3})	ρ_g (g cm^{-3})	$\Delta\rho/\rho_g$	$\sigma_{RT} \times 10^{-4}$ (S m^{-1})	ε' at 2 MHz (tan δ)	κ_{RT} (W m^{-1} K^{-1})
a_g[TPrA][Mn(dca)$_3$]	6.65 (±0.08)	1.237 (±0.005)	1.335 (±0.006)	0.073 (±0.005)	0.02	32 (0.03)	0.258
a_g[TPrA][Fe(dca)$_3$]	5.85 (±0.09)	1.225 (±0.004)	1.326 (±0.002)	0.076 (±0.003)	25.0	–[a]	0.234
a_g[TPrA][Co(dca)$_3$]	6.98 (±0.07)	1.245 (±0.005)	1.283 (±0.004)	0.030 (±0.004)	0.66	30 (0.07)	0.228

[a]Unsaturated at the limit of the instrumental frequency, 2 MHz. Details of dielectric permittivity values can be found in the Supplementary Methods and Supplementary Figs. 54 and 55. E, Young's modulus; ρ_c, crystal density; ρ_g, glass density; $\Delta\rho/\rho_g$, crystal–glass network density deficit; σ_{RT}, electrical conductivity at room temperature; ε' (tan δ), dielectric permittivity (dielectric loss); κ_{RT}, thermal conductivity at room temperature.

finding absolute values of thermal conductivity at room temperature (κ_{RT}) of 0.258 W m^{-1} K^{-1} for a_g[TPrA][Mn(dca)$_3$], 0.234 W m^{-1} K^{-1} for a_g[TPrA][Fe(dca)$_3$] and 0.228 W m^{-1} K^{-1} for a_g[TPrA][Co(dca)$_3$] (Fig. 4d, Supplementary Fig. 53). The similar values, despite the difference in M(0) content, suggest that the thermal insulating organic component predominates over the thermal conductive metallic components. These values are lower than those of the recently reported lead halide perovskites (~0.40–0.50 W m^{-1} K^{-1})[36,37], cobalt formate perovskite (~1.3 W m^{-1} K^{-1})[38], Zn–MOF-5 (~0.32 W m^{-1} K^{-1})[39] and ZIF-8 thin film (~0.33 W m^{-1} K^{-1})[40] systems. They are also significantly lower compared to other glass architectures, for example doped silicates or borosilicates (~1 W m^{-1} K^{-1})[41].

Discussion

The relatively low melting points of the HOIPs (T_m ~250 °C), together with low activation energies, E_a, for the glass transition,

suggests a greater accessibility and processability of the liquid state compared to inorganics and ZIF glasses.

The similarity of the melting mechanism, that is the rare event of metal–linker bond breakage, to that observed in inorganic solids and ZIFs, is in accordance with both Lindemann's law and the dominant route to glass formation being the quenching of the liquid state[42,43]. Some metal reduction and dca decomposition may explain the absence of glass recrystallization, whilst the glass densities are notably also substantially higher than those of existing ZIF glasses[44], although they are still coupled to similar values of the Young's modulus (E ~6–7 GPa, Table 2, Methods, Supplementary Fig. 56). This suggests the dominant role of coordination bonding in determining the intermediate compliance of both MOF- and hybrid perovskite-derived glasses between organics and inorganics (Fig. 5a)[18].

The glasses are set aside from existing coordination-polymer glasses by their chemical tunability, together with a range of
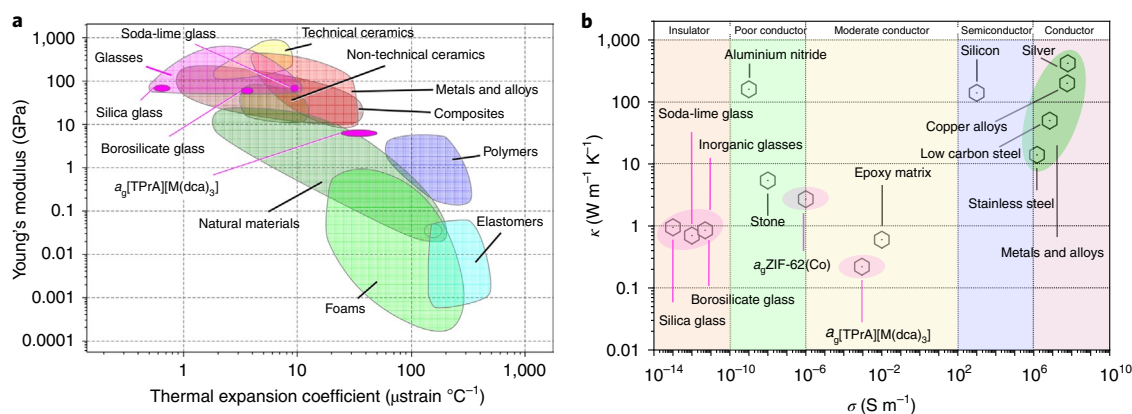
Fig. 5 | Comparison of physical properties of melt-quenched glasses with various materials. a, An Ashby plot of Young's modulus (E) versus thermal expansion coefficient (α). Representative values of α were calculated from the data in Fig. 1c. **b**, An Ashby plot of thermal conductivity (κ) versus electrical conductivity (σ) at 300 K. Both **a** and **b** show the comparison of the glasses with various classes of materials including other glass types. Data in Ashby plots collated using the CES EduPack software[50].

potentially useful properties. These include moderate electrical conductivities at room temperature (10^{-3}–10^{-5} S m^{-1}), which are twice as large as those of various cation-doped inorganic ion-conducting silicate, borosilicate[45] and also ZIF-based glasses (for example a_gZIF-62(Co) ~0.8×10^{-6} S m^{-1}, Supplementary Fig. 57). They are also much larger than the electrical conductivity of the semiconductor lead halide perovskites (8.0×10^{-6} S m^{-1})[37]. Coupled with their very low values of thermal conductivity at room temperature (~0.2 W m^{-1} K^{-1}), which are also much lower than those in chemically similar ZIF glasses (for example a_gZIF-62(Co) ~2.7 W m^{-1} K^{-1}, Supplementary Fig. 57), these properties may suggest possible uses in thermoelectric settings such as efficient energy conversion and waste-heat power generation (Fig. 5b)[46].

The dca-containing family of perovskites themselves offer great potential for developing structure–property relationships by changing the 'A' site ammonium cation, or by utilizing different transition metals on the 'B' site(s), whilst the melting of HOIPs containing different organic linkers such as azides or hypophosphites will also be of interest[7]. This is in addition to studies of the effect of defects (near ubiquitous in the wider HOIP family) on melting and research into the interplay between metal reduction, ligand decomposition/rearrangement, recrystallization and glass-formation events. These studies may be key in raising electrical conductivities to approach those of the best inorganic (~(10^3–10^6) S m^{-1})[47] and organic (~(10^{-3}–10^5) S m^{-1})[48] thermoelectric materials.

Online content

Any methods, additional references, Nature Research reporting summaries, source data, extended data, supplementary information, acknowledgements, peer review information; details of author contributions and competing interests; and statements of data and code availability are available at https://doi.org/10.1038/s41557-021-00681-7.

References

1. Mitzi, D. B. Introduction: Perovskites. *Chem. Rev.* **119**, 3033–3035 (2019).
2. Li, W. et al. Chemically diverse and multifunctional hybrid organic–inorganic perovskites. *Nat. Rev. Mater.* **2**, 16099 (2017).
3. Li, W., Stroppa, A., Wang, Z.-M. & Gao, S. *Hybrid Organic-Inorganic Perovskites* (Wiley, 2020).
4. Burschka, J. et al. Sequential deposition as a route to high-performance perovskite-sensitized solar cells. *Nature* **499**, 316–319 (2013).
5. Lee, M. M. et al. Efficient hybrid solar cells based on meso-superstructured organometal halide perovskites. *Science* **338**, 643–647 (2012).
6. Jain, P. et al. Multiferroic behavior associated with an order–disorder hydrogen bonding transition in metal–organic frameworks (MOFs) with the perovskite ABX$_3$ architecture. *J. Am. Chem. Soc.* **131**, 13625–13627 (2009).
7. Wu, Y. et al. [Am]Mn(H$_2$POO)$_3$: a new family of hybrid perovskites based on the hypophosphite ligand. *J. Am. Chem. Soc.* **139**, 16999–17002 (2017).
8. Bermudez-Garcia, J. M. et al. Role of temperature and pressure on the multisensitive multiferroic dicyanamide framework [TPrA][Mn(dca)$_3$] with perovskite-like structure. *Inorg. Chem.* **54**, 11680–11687 (2015).
9. Saparov, B. & Mitzi, D. B. Organic–inorganic perovskites: structural versatility for functional materials design. *Chem. Rev.* **116**, 4558–4596 (2016).
10. Egger, D. A., Rappe, A. M. & Kronik, L. Hybrid organic–inorganic perovskites on the move. *Acc. Chem. Res.* **49**, 573–581 (2016).
11. Wang, Y. H. et al. Pressure-induced phase transformation, reversible amorphization, and anomalous visible light response in organolead bromide perovskite. *J. Am. Chem. Soc.* **137**, 11144–11149 (2015).
12. Ou, T. J. et al. Visible light response, electrical transport, and amorphization in compressed organolead iodine perovskites. *Nanoscale* **8**, 11426–11431 (2016).
13. Mitzi, D. B. Synthesis, crystal structure, and optical and thermal properties of (C$_4$H$_9$NH$_3$)$_2$MI$_4$ (M=Ge, Sn, Pb). *Chem. Mater.* **8**, 791–800 (1996).
14. Gaillac, R. et al. Liquid metal–organic frameworks. *Nat. Mater.* **16**, 1149–1154 (2017).
15. Bermudez-Garcia, J. M. et al. Multiple phase and dielectric transitions on a novel multi-sensitive [TPrA][M(dca)$_3$] (M: Fe^{2+}, Co^{2+} and Ni^{2+}) hybrid inorganic–organic perovskite family. *J. Mater. Chem. C* **4**, 4889–4898 (2016).
16. Umeyama, D. et al. Reversible solid-to-liquid phase transition of coordination polymer crystals. *J. Am. Chem. Soc.* **137**, 864–870 (2015).
17. Bermudez-Garcia, J. M. et al. A simple in situ synthesis of magnetic M@ CNTs by thermolysis of the hybrid perovskite [TPrA][M(dca)$_3$]. *New J. Chem.* **41**, 3124–3133 (2017).
18. Qiao, A. et al. A metal–organic framework with ultrahigh glass-forming ability. *Sci. Adv.* **4**, eaao6827 (2018).
19. Pell, A. J., Pintacuda, G. & Grey, C. P. Paramagnetic NMR in solution and the solid state. *Prog. Nucl. Magn. Reson. Spectrosc.* **111**, 1–271 (2019).
20. Ishii, Y., Wickramasinghe, N. P. & Chimon, S. A new approach in 1D and 2D ^{13}C high-resolution solid-state NMR spectroscopy of paramagnetic organometallic complexes by very fast magic-angle spinning. *J. Am. Chem. Soc.* **125**, 3438–3439 (2003).
21. Kervern, G., Pintacuda, G. & Emsley, L. Fast adiabatic pulses for solid-state NMR of paramagnetic systems. *Chem. Phys. Lett.* **435**, 157–162 (2007).
22. Gougeon, R. et al. High-resolution solid-state nuclear magnetic resonance study of the tetrapropylammonium template in a purely siliceous MFI-type zeolite. *Magn. Reson. Chem.* **36**, 415–421 (1998).
23. Hing, A. W., Vega, S. & Schaefer, J. Transferred-echo double-resonance NMR. *J. Magn. Reson.* **96**, 205–209 (1992).
24. Tucker, M. C. et al. Hyperfine fields at the Li site in LiFePO$_4$-type olivine materials for lithium rechargeable batteries: a ^{7}Li MAS NMR and SQUID study. *J. Am. Chem. Soc.* **124**, 3832–3833 (2002).
25. Tauber, K., Dani, A. & Yuan, J. Y. Covalent cross-linking of porous poly(ionic liquid) membrane via a triazine network. *Acs Macro. Lett.* **6**, 1–5 (2017).
26. Kroke, E. et al. Tri-s-triazine derivatives. Part I. From trichloro-tri-s-triazine to graphitic C$_3$N$_4$ structures. *New J. Chem.* **26**, 508–512 (2002).

27. Silverstein, R. M., Webster, F. X., Kiemle, D. J. & Bryce, D. L. *Spectrometric Identification of Organic Compounds* 8th edn (Wiley, 2014).
28. Orgel, L. E. Spectra of transition-metal complexes. *J. Chem. Phys.* **23**, 1004–1014 (1955).
29. Bo, S. H. et al. Thin-film and bulk investigations of $LiCoBO_3$ as a Li-ion battery cathode. *ACS Appl. Mater. Interfaces* **6**, 10840–10848 (2014).
30. Schlueter, J. A., Manson, J. L. & Geiser, U. Structural and magnetic diversity in tetraalkylammonium salts of anionic $M[N(CN)_2]_3^-$ (M = Mn and Ni) three-dimensional coordination polymers. *Inorg. Chem.* **44**, 3194–3202 (2005).
31. Chakravarty, C., Debenedetti, P. G. & Stillinger, F. H. Lindemann measures for the solid-liquid phase transition. *J. Chem. Phys.* **126**, 204508 (2007).
32. Leo, C. J., Rao, G. V. S. & Chowdari, B. V. R. Fast ion conduction in the Li-analogues of Nasicon, $Li_{1+x}[(Ta_{1-x}Ge_x)Al](PO_4)_3$. *J. Mater. Chem.* **12**, 1848–1853 (2002).
33. Chowdari, B. V. R., Yoo, H.-L., Choi, G. M. & Lee, J.-H. *Solid State Ionics: The Science and Technology of Ions in Motion* (World Scientific, 2004).
34. Snyder, G. J. & Toberer, E. S. Complex thermoelectric materials. *Nat. Mater.* **7**, 105–114 (2008).
35. Bell, L. E. Cooling, heating, generating power, and recovering waste heat with thermoelectric systems. *Science* **321**, 1457–1461 (2008).
36. Pisoni, A. et al. Ultra-low thermal conductivity in organic–inorganic hybrid perovskite $CH_3NH_3PbI_3$. *J. Phys. Chem. Lett.* **5**, 2488–2492 (2014).
37. Ye, T. et al. Ultra-high Seebeck coefficient and low thermal conductivity of a centimeter-sized perovskite single crystal acquired by a modified fast growth method. *J. Mater. Chem. C* **5**, 1255–1260 (2017).
38. Gunatilleke, W. D. C. B. et al. Thermal conductivity of a perovskite-type metal–organic framework crystal. *Dalton Trans.* **46**, 13342–13344 (2017).
39. Huang, B. L. et al. Thermal conductivity of a metal-organic framework (MOF-5): Part II. Measurement. *Int. J. Heat Mass Transfer* **50**, 405–411 (2007).
40. Cui, B. Y. et al. Thermal conductivity of ZIF-8 thin-film under ambient gas pressure. *ACS Appl. Mater. Interfaces* **9**, 28139–28143 (2017).
41. Bansal, N. P. & Doremus, R. H. *Thermal Conductivity* (Elsevier, 1986).
42. Debenedetti, P. G. & Stillinger, F. H. Supercooled liquids and the glass transition. *Nature* **410**, 259–267 (2001).
43. Angell, C. A. Formation of glasses from liquids and biopolymers. *Science* **267**, 1924–1935 (1995).
44. Bennett, T. D. et al. Melt-quenched glasses of metal–organic frameworks. *J. Am. Chem. Soc.* **138**, 3484–3492 (2016).
45. Bansal, N. P. & Doremus, R. H. *Electrical Conductivity* (Elsevier, 1986).
46. Wu, Y. et al. Hypophosphite hybrid perovskites: a platform for unconventional tilts and shifts. *Chem. Commun.* **54**, 3751–3754 (2018).
47. Gaultois, M. W. et al. Data-driven review of thermoelectric materials: performance and resource considerations. *Chem. Mater.* **25**, 2911–2920 (2013).
48. Russ, B. et al. Organic thermoelectric materials for energy harvesting and temperature control. *Nat. Rev. Mater.* **1**, 16050 (2016).
49. Menard, K. P. & Menard, N. R. in *Encyclopedia of Polymer Science and Technology* 1–33 (Wiley, 2015).
50. CES EduPack 2019 Software (Granta Design, 2019).

Methods

Synthesis of hybrid perovskites. *Reagents.* $Mn(NO_3)_2 \cdot 4H_2O$ (98.5%, Sigma-Aldrich), $FeCl_2 \cdot 4H_2O$ (98%, Sigma-Aldrich), $Co(NO_3)_2 \cdot 6H_2O$ (98%, Sigma-Aldrich), (TPrA)Br (98%, Aldrich), Na(dca) (96%, Sigma-Aldrich), imidazole (99%, Sigma-Aldrich), benzimidazole (98%, Sigma-Aldrich) and *N,N*-dimethylformamide (99.8%, Fisher Chemical) were purchased as indicated and were used as received.

Procedure. The synthesis reported in the literature was followed[8,15,30]. Specifically, 10 ml of an aqueous solution of metal salt (Mn^{2+}, Fe^{2+}, Co^{2+}) (2 mmol) was placed at the bottom of a thin crystallization tube and layered with a mixture of a solution of Na(dca) (6 mmol in 10 ml of water) and (TPrA)Br (2 mmol in 10 ml of ethanol). Block-shaped single crystals were obtained from the mother liquor after one week of slow evaporation in an open atmosphere. They were colourless (Mn), pale yellow (Fe) and pink (Co), respectively.

We note that the Fe(II) and Co(II) analogues each exhibit three first-order structural phase transitions, arising from a displacement of TPrA cations and order–disorder transitions of both TPrA cations and dca anions. The Mn(II) analogue shows type-I multiferroism[8], due to coexistence of antiferroelectric and antiferromagnetic order. A high sensitivity to applied external pressure facilitates a giant caloric effect of 37.0 J kg^{-1} K^{-1} (ref. [51]). This occurs under very low applied pressures ($P < 7$ MPa) just above room temperature with a calculated barocaloric tunability ($\partial T_t / \partial P$) of 23.1 K kbar^{-1} (refs. [51,52]).

Synthesis of zeolitic imidazolate framework glass. The method previously reported by Henke and colleagues was used here[53]. Specifically, $Co(NO_3)_2 \cdot 6H_2O$ (4.0 mmol, 1.2 g) and a mixture of 7 equiv. imidazole (0.786 g, 11.55 mmol) and 1 equiv. benzimidazole (0.196 mg, 1.66 mmol) were dissolved in 90 ml *N,N*-dimethylformamide. The obtained solution was divided into 10 portions (9 ml) which were transferred to 10 borosilicate glass vials (12 ml). The tightly sealed reaction vials were transferred to a preheated oven (at 130 °C) for 7 days. After cooling to room temperature, the reaction volumes were recombined, filtered and washed three times with 20 ml *N,N*-dimethylformamide. Deep purple ZIF-62(Co) crystals were obtained as large, truncated, octahedrally shaped single crystals. The as-synthesized material was dried at 200 °C under dynamic vacuum (pressure ~10^{-3} mbar) for 20 h to evacuate the sample. This sample was then ground by hand, before heating in the differential scanning calorimeter to 475 °C under an argon atmosphere at a heating rate of 10 °C min^{-1}. The liquid formed was then cooled to room temperature (cooling rate 10 °C min^{-1}) to obtain the glass.

Thermal analysis. TGA was carried out on a SDT-Q600 apparatus (TA Instruments). Data were collected in the range 25–400 °C at a scan rate of 10 °C min^{-1} under an argon atmosphere.

DSC measurements were conducted using a Netzsch 214 Polyma instrument. Samples were hand ground, placed in an aluminium pan and heated up to their respective melting offset temperature at a heating rate of 10 °C min^{-1} under an argon atmosphere. To obtain the glass transition, the melted solids were cooled to 60 °C at 10 °C min^{-1} unless otherwise specified, and then reheated at 10 °C min^{-1} up to the target temperature.

Simultaneous differential scanning calorimeter/thermogravimetric analyser (SDT) measurements were conducted using a TA Q600 instrument, under argon flow at a heating rate of 10 °C min^{-1}. In each case ~10 mg of ground sample was placed into a 70 µl alumina crucible.

Preparation of glasses in DSC and SDT measurements. a_g[TPrA][Mn(dca)$_3$]: A ground sample of [TPrA][Mn(dca)$_3$] was heated at 10 °C min^{-1} to 277 °C, then cooled under an argon atmosphere (100 ml min^{-1} flow rate), before cooling back to room temperature at ~3 °C min^{-1}. Samples formed in the SDT instrument were used for NMR, XPS, HRMS, Fourier transform infrared (FTIR) and PDF measurements.

a_g[TPrA][Fe(dca)$_3$]: Crystals of [TPrA][Fe(dca)$_3$] were cooled from 269 °C under an argon atmosphere (100 ml min^{-1} flow rate) at a rate of ~10 °C min^{-1}. Samples formed in the SDT instrument were used for NMR, XPS, HRMS, FTIR and PDF measurements.

a_g[TPrA][Co(dca)$_3$]: A ground sample of [TPrA][Co(dca)$_3$] was rapidly cooled from 264 °C under an argon atmosphere. A cooling rate of ~30 °C min^{-1} was used, that is the cooling rate attained by the instrument on cooling back to room temperature without a given ramp rate. Samples formed in the DSC instrument were used for NMR, XPS, HRMS, FTIR and PDF measurements.

In the cases of a_g[TPrA][Mn(dca)$_3$] and a_g[TPrA][Fe(dca)$_3$], partial recrystallization was observed on cooling the melt from 263 and 271 °C, respectively, indicating the complex interplay between decomposition, recrystallization and vitrification (Supplementary Fig. 6).

Thermomechanical analysis. For a_g[TPrA][Mn(dca)$_3$] and a_g[TPrA][Fe(dca)$_3$], dense flat pieces of quenched-glass samples were used to determine the coefficient of thermal expansion and T_f values. However, due to the irregular shape of the a_g[TPrA][Co(dca)$_3$], a pelletized glass sample was used. In this technique, the linear expansion of the glasses was measured as a function of temperature at a standard TMA heating rate of 5 °C min^{-1}. A standard force of 10 mN was applied under an N_2 atmosphere using the dilatometer on a Q400 TMA instrument (TA Instruments).

Dynamic mechanical analysis. Glass transition relaxation dynamics were investigated using a TA instruments DMA-Q800 dynamic mechanical analyser (Supplementary Fig. 58). To perform the measurements, amorphous powders were wrapped in aluminium foil in a rectangular sample geometry. The sample geometry was pre-calibrated with polycarbonate reference. Specimens of equal mass and of even thickness (dimensions of ~35.0 mm × 12.8 mm × 3.2 mm) and with parallel sides were prepared. A slow heating rate of 2 °C min^{-1} was applied to minimize the thermal fluctuation and dipolar coupling (low loss/heat dissipation) with an applied frequency varying from 1–3 Hz. The single cantilever measurement mode was used.

The out-of-phase component (loss modulus) and the loss (tan δ) show a strong broad peak close to the softening point. Broad peaks, as witnessed here, have also been observed in DMA of other materials such as highly cross-linked polymers. The loss modulus is considered more reliable for the accurate determination of T_g due to the very low storage moduli of the glasses[54].

Powder X-ray diffraction. Ambient temperature: X-ray powder diffraction patterns were recorded ($2\theta = 10°–60°$) on a Bruker D8 Advance diffractometer (equipped with a LynxEye EX linear position sensitive detector) in Bragg–Brentano geometry using a Cu Kα ($\lambda = 1.540598$ Å) source fitted with a Ni 0.012 mm filter. Data were collected at a 2θ step size of 0.02° with a counting time of 10 s per step.

Scanning electron microscopy. The surface morphologies of the melt-quenched glass samples were investigated using a high-resolution scanning electron microscope, FEI Nova Nano SEM 450, operated at 5 kV (working distance ~5.5 mm). Palladium sputtering was used to reduce charging of the specimen.

NMR. *Solid-state NMR.* Experiments were performed on a 9.4 T Bruker Avance III HD spectrometer equipped with a 1.3 mm HXY MAS probe in double resonance mode. The ^{1}H channel was tuned to $\nu_0(^1H) = 400.13$ MHz and the X channel was tuned to $\nu_0(^{13}C) = 100.61$ MHz. Spectra were recorded under an optimized approach for paramagnetic systems combining very fast MAS (ref. [20]) with double adiabatic echo detection and shaped pulses[21]. All NMR spectra were recorded at a spinning rate of 60 kHz, corresponding to a sample temperature of at least ~50–55 °C (as measured from the ^{79}Br NMR chemical shift and spin-lattice relaxation rate change of KBr (ref. [55])) with no temperature regulation. Pulses were applied at a radiofrequency field of 200 kHz at an offset of 0 ppm for [TPrA][Mn(dca)$_3$] and 2,985 ppm for both [TPrA][Fe(dca)$_3$] and [TPrA][Co(dca)$_3$]. A double adiabatic echo pulse sequence was employed to record the MAS NMR spectra and used square $\pi/2$ excitation pulses of duration 1.25 µs and rotor synchronized short (50 µs) high powered adiabatic tanh/tan (SHAPs) inversion pulses sweeping through 10 MHz to refocus the chemical shift evolution;[21] this sequence showed an approximate two-fold increase in signal intensity versus the double echo pulse sequence employing square $\pi/2$ and π pulses, largely in agreement with the literature[21]. TEDOR experiments[21,23] were performed with an optimized recoupling time equal to 3 rotor periods (50 µs) and adiabatic SHAPs inversion pulses were applied to the ^{1}H channel to improve polarization transfer[24]. TEDOR experiments were performed with a recycle delay of $1.3 \times {}^1$H T_1 to ensure maximum signal-to-noise ratio per unit time. No ^{1}H decoupling was used during any solid-state NMR ^{13}C acquisition. The ^{13}C MAS NMR spectra were typically accumulated with 2 million scans with recycle delays of 0.01 s which were found to be long enough to avoid saturation. Note that the ^{13}C signal intensities do not directly relate to the number of carbons present, as the optimized data acquisition strategy is not quantitative due to the likely large differences in the ^{13}C T_2' (transverse magnetization decay time constant with refocused inhomogeneous broadening) values. ^{1}H spectra were referenced to H_2O at 4.8 ppm and ^{13}C spectra were referenced to the CH peak of adamantane at 29.45 ppm, corresponding to tetramethylsilane at 0 ppm (ref. [56]). All samples for solid state NMR were finely ground.

No ^{13}C resonance outside the standard diamagnetic 200 to 0 ppm region was observed in crystalline [TPrA][Mn(dca)$_3$] (Supplementary Fig. 12). This prompted us to explore the use of a ^{13}C-edited experiment to identify the dca carbon, which is best achieved in these systems using a ^{1}H-^{13}C double resonance TEDOR NMR experiment[21,23]. In this experiment, only protonated carbons were observed and the corresponding ^{1}H-^{13}C TEDOR NMR spectrum of [TPrA][Mn(dca)$_3$] unambiguously showed the disappearance of the 3–7 ppm signal which is therefore assigned to the carbon of the dca anion ligand.

The spectral deconvolution of [TPrA][Co(dca)$_3$] and [TPrA][Fe(dca)$_3$] in Supplementary Figs. 15 and 16 shows three resonances in the 200 to −100 ppm region corresponding to three carbon environments within the TPrA molecule in the unit cell[15]. The spectral deconvolution of [TPrA][Mn(dca)$_3$] in Supplementary Fig. 17 shows three resonances corresponding to the N*C*H$_2$ within the TPrA molecule and two resonances for the N*C*N within the dca ligand in a 2:1 ratio. This is in agreement with the expected number of carbon environments in the unit cell for this compound[8]. The limited resolution does not permit the *C*H$_2$*C*H$_3$ and *C*H$_3$ groups to be distinguished from one another.

Therefore, the NMR spectra of the crystalline compounds are consistent with their crystal structures[8,15]. Specifically, they support the existence of one TPrA cation and two dca anions in the asymmetric unit cell within the orthorhombic *Ibam* (centrosymmetric) space group of [TPrA][Fe(dca)$_3$] and [TPrA][Co(dca)$_3$][15] and the presence of three independent ions in the tetragonal space group $P\bar{4}2_1c$ of [TPrA][Mn(dca)$_3$] at the temperature of the MAS NMR detection (ref. [8]).

Liquid-phase NMR. Experiments were performed on a 9.4 T Bruker Avance III HD spectrometer equipped with a 5 mm BBFO probe. Digested samples were prepared by dissolving ~8 mg of sample in 100 μl of 35 wt% DCl in D$_2$O then dissolving the mixture in 500 μl DMSO-d$_6$. Deuterium was used to remove the ^{1}H signal from the solvent, although the D$_2$O still contained some H$_2$O. On digestion of the ground samples, pink [TPrA][Co(dca)$_3$], off-white [TPrA][Mn(dca)$_3$] and yellow-ish/off-white [TPrA][Fe(dca)$_3$] changed colour in solution to blue (likely corresponding to tetrahedral (CoCl$_4$)$^{2-}$), colourless and yellow, respectively. ^{1}H chemical shifts are reported relative to the corresponding signals of residual protons in DMSO-d$_6$ at 2.50 ppm. ^{13}C spectra were recorded with ^{1}H decoupling and are reported relative to the DMSO-d$_6$ signal at 39.50 ppm ($^1J_{CD}$ = 21 Hz was not resolved in the Fe and Co samples as this signal was too broad). In the Supplementary Information, br indicates that the signals are broad. The ^{1}H and ^{13}C spectra were recorded with 16 and 960–4,000 scans, respectively.

On acidic sample digestion, decoordination of the TPrA and dca ligands readily occurs as shown by the ^{1}H and ^{13}C liquid-phase NMR spectra (Supplementary Figs. 19–24). These spectra also show a range of broadening that depends on the strength of the paramagnetism, which is largely a function of the hyperfine coupling to the paramagnetic ion. Starting with the most resolved NMR spectra for the crystalline and glass-quenched Co samples, the NMR spectra of the TPrA ligand are straightforward to assign based on chemical shifts and electron withdrawing of the nitrogen atoms. Some scalar *J* couplings are observed in the ^{1}H NMR spectra of both [TPrA][Co(dca)$_3$] and a_g[TPrA][Co(dca)$_3$]. Cyanamide exists as two aminonitrile–carbodiimide tautomers, which for the dca ligand translates into the equilibrium depicted in Supplementary Scheme 1. In this equilibrium the ^{1}H NMR spectra of both Co materials display a single resonance at ~8 ppm for the NH group that is likely to be due to an exchange between the tautomers at room temperature under acidic conditions. The ^{13}C NMR spectrum of [TPrA][Co(dca)$_3$] shows two additional resonances for TPrA at around 150 and 110 ppm that can be attributed to the carbodiimide and nitrile carbons, respectively[27]. Only the latter resonance is observed in a_g[TPrA][Co(dca)$_3$] (the signal of the nitrile carbon is likely to be in the noise level). This demonstrates the presence of dca, which is further confirmed by HRMS data (below).

The ^{1}H NMR spectra of the Fe and Co samples are significantly broadened by hyperfine coupling (especially for Co^{2+}). However, all four resonances for TPrA and the dca tautomers as described above are clearly observed, indicating that the quenched-glass samples contain both ligands. Whilst the ^{13}C NMR spectrum of [TPrA][Fe(dca)$_3$] is virtually identical to the corresponding Mn one, the signals arising from the dca ligand are just above the noise level. These are challenging to observe in the corresponding glasses, despite extended experimental times. Nevertheless, the NH resonance in the more sensitive ^{1}H spectra conclusively confirms the presence of the dca ligand.

HRMS. HRMS data were recorded on an Agilent 6540A Quadrupole-Time-Of-Flight (TOF) mass spectrometer using electrospray ionization (ESI) in either negative or positive mode (Supplementary Figs. 25–30).

Digested samples were prepared by dissolving ~1 mg of sample in 1 ml of either H$_2$O (with or without 50 μl of HCO$_2$H) or a H$_2$O:CH$_3$OH mixture in a 1:1 ratio (v/v) to ensure dissolution. Either H$_2$O or a H$_2$O:CH$_3$OH mixture in an 8:2 ratio (v/v) (for the samples dissolved with CH$_3$OH), all containing 0.1% HCO$_2$H, were used as the eluent.

m/z found in ESI$^-$ at 69.9961 and 112.9853 are trifluoromethane ion (calculated for (CF$_3$$^-$) 68.9952) and trifluoroacetic acid ion (calculated for (CF$_3$CO$_2$$^-$) 112.9850), respectively, as part of the set of reference ions used for HRMS were subtracted from the data for clarity.

ESI$^+$ data show a very strong and clear signal for the [TPrA]$^+$ molecular ion (*m/z* calculated 186.2222, found 186.2214–186.2222) in all crystalline and melt-quenched Mn, Fe and Co materials. ESI$^-$ data highlight that the dca$^-$ ion is present either as its molecular ion (*m/z* calculated 66.0092, found 66.0101–66.0104), an H$_2$O adduct (*m/z* calculated 84.0198, found 84.0203–84.0206) or a [Mn + 3 × dca]$^-$ complex (*m/z* calculated 252.9657, found 252.9654). These HRMS data undoubtedly demonstrate that dca and TPrA species remain largely intact on melting.

FTIR study. FTIR spectra for a ground crystal, prior to melting and glass samples, were collected in transmittance mode on a Bruker Tensor 27 spectrometer.

Diffuse reflectance UV-Vis study. A Perkin Elmer Lambda 750 spectrophotometer was used to measure the solid-state diffuse reflectance UV-vis spectra. Spectra for all ground crystalline and glass powder samples were recorded in the range 200–800 nm. A BaSO$_4$ matrix was used as a reference. Absorbances were estimated using the Kubelka−Munk transform function $\frac{\alpha KM}{s} = \frac{(1-R)^2}{2R}$, where

R is the measured diffuse reflectance and *s* is an unknown sample scattering coefficient[57].

Magnetic study. A SQUID MPMS 3 instrument was used to conduct the magnetic measurements of hybrid perovskite crystals and glasses. The temperature variation of field-cooled susceptibility (*M–T*) data was collected at 500 Oe magnetic field over a temperature range 2–300 K. Magnetization as a function of magnetic field (*M–H*) was measured at 300 K, with the magnetic field varying by up to 7 T. Samples were placed in a light-weight homogeneous quartz tube to minimize the background noise and stray field effects. The magnetic data were corrected for the diamagnetic contribution from the quartz sample holder and the intrinsic diamagnetism of the samples using Pascal's constants[58].

XPS spectroscopy. Ground powder samples of crystals and glasses were used to perform the measurements using an Escalab 250Xi instrument together with a monochromatic Al Kα X-ray source. Inert ultra-high vacuum conditions were also applied.

X-ray total scattering experiments. X-ray data were collected at the I15-1 beamline at the Diamond Light Source, UK (λ = 0.161669 Å, 76.7 keV). Samples were loaded into borosilicate capillaries of 1.17 mm inner diameter. Data on the samples, empty instrument and capillary were collected in the region ~0.4 < *Q* < ~26 Å^{-1}, where *Q* is a scattering vector. Corrections for background, multiple scattering, container scattering, Compton scattering, fluorescence and absorption were performed using the GudrunX program[59,60].

Network density measurements. The physical densities of all hybrid perovskite crystals and glasses were measured using a Micromeritics Accupyc 1340 helium pycnometer. The typical mass of sample used for each test was about 80 mg. The reported values were averaged over ten measurements.

First-principles molecular dynamics. The behaviour of [TPrA][Mn(dca)$_3$] as a function of temperature was studied using density functional theory based molecular dynamics simulations using the Quickstep module[61] of the CP2K software package (available online at http://www.cp2k.org). The simulated configuration was the tetragonal crystallographic unit cell, which contained 456 atoms with cell parameters *a* = *b* = 16.275 Å, *c* = 17.423 Å and α = β = γ = 90° (Supplementary Methods, Results and Discussion).

Electrical conductivity measurements. Room-temperature a.c. conductivity measurements were performed with an Agilent E4980A Precision LCR meter capable of measuring in the frequency range 20 Hz–2 MHz (Supplementary Methods, Results and Discussion).

Thermal conductivity measurements. Thermal conductivities of the glasses were measured with Quantum Design's Physical Property Measurement System (DynaCool) using the thermal transport option (TTO) mode in a two-probe lead configuration (Supplementary Methods, Results and Discussion, Supplementary Fig. 59).

Elemental characterization from CHN analysis. The elemental compositions were obtained using a CHN analyser (Supplementary Table 3). Compared to the crystalline states, a minor decrease in the concentration of carbon (~0.4%) and nitrogen (~0.3%) was observed in the glasses. Measurements on ground powder samples were performed using a CE440 Elemental Analyzer (Exeter Analytical).

Elemental characterization from scanning electron microscopy–energy-dispersive X-ray analysis. The weight percentage of N and M contents was evaluated for the glasses from the scanning electron microscopy–energy-dispersive X-ray spectra (Supplementary Fig. 60, Supplementary Table 3). Nitrogen ratios were found to vary slightly compared to the XPS and CHN results. The spectra were recorded with a high energy electron beam (~10 keV).

Nanoindentation. Dense flat pieces of quenched-glass samples were mounted with epoxy resin and finely polished prior to nanoindentation tests. An MTS Nanoindenter XP instrument was used under dynamic displacement controlled mode at a constant strain rate of 0.05 s^{-1} at ambient conditions. Deformation of the polished samples was made using a Berkovich diamond tip pre-calibrated with fused silica. A Poisson's ratio of ν = 0.2 was used in accordance with the literature[44]. Use of ν = 0.34, as reported by To et al.[62] led to changes in *E* (Young's modulus) of <1%. Absolute values of *E* were determined from the variable indentation depth scans to a maximum surface penetration of 1,000 nm and are shown with error bars over 20 consecutive scans.

Data availability

Representative input files for the molecular dynamics simulations are available online in our data repository at https://github.com/fxcoudert/citable-data. The experimental data that support the findings of this study (characterization and analytical data for both crystalline and glass materials, structural refinements,

a.c. electrical conductivity experiments and thermal conductivity measurements, source data for all experimental Supplementary figures) are available as Supplementary Information and in Symplectic Elements with the identifier https://doi.org/10.17863/CAM.63032.

References

51. Bermudez-Garcia, J. M. et al. Giant barocaloric tunability in $[(CH_3CH_2CH_2)_4N]Cd[N(CN)_2]_3$ hybrid perovskite. *J. Mater. Chem. C* **6**, 9867–9874 (2018).

52. Bermudez-Garcia, J. M. et al. Giant barocaloric effect in the ferroic organic-inorganic hybrid $[TPrA][Mn(dca)_3]$ perovskite under easily accessible pressures. *Nat. Commun.* **8**, 15715 (2017).

53. Frentzel-Beyme, L. et al. Porous purple glass – a cobalt imidazolate glass with accessible porosity from a meltable cobalt imidazolate framework. *J. Mat. Chem. A* **7**, 985–990 (2019).

54. Li, G., Lee-Sullivan, P. & Thring, R. W. Determination of activation energy for glass transition of an epoxy adhesive using dynamic mechanical analysis. *J. Therm. Anal. Calorim.* **60**, 377–390 (2000).

55. Thurber, K. R. & Tycko, R. Measurement of sample temperatures under magic-angle spinning from the chemical shift and spin-lattice relaxation rate of ^{79}Br in KBr powder. *J. Magn. Reson.* **196**, 84–87 (2009).

56. Morcombe, C. R. & Zilm, K. W. Chemical shift referencing in MAS solid state NMR. *J. Magn. Reson.* **162**, 479–486 (2003).

57. Fuller, M. P. & Griffiths, P. R. Diffuse reflectance measurements by infrared Fourier transform spectrometry. *Anal. Chem.* **50**, 1906–1910 (1978).

58. Bain, G. A. & Berry, J. F. Diamagnetic corrections and Pascal's constants. *J. Chem. Educ.* **85**, 532–536 (2008).

59. Soper, A. K. *GudrunN and GudrunX: Programs for Correcting Raw Neutron and X-ray Diffraction Data to Differential Scattering Cross Section*. Technical Report RAL-TR-2011-013 (2011).

60. Soper, A. K. & Barney, E. R. Extracting the pair distribution function from white-beam X-ray total scattering data. *J. Appl. Crystallogr.* **44**, 714–726 (2011).

61. VandeVondele, J. et al. QUICKSTEP: fast and accurate density functional calculations using a mixed Gaussian and plane waves approach. *Comput. Phys. Commun.* **167**, 103–128 (2005).

62. To, T. et al. Fracture toughness of a metal–organic framework glass. *Nat. Commun.* **11**, 2593 (2020).

Author contributions

B.K.S. and T.D.B. designed the project. A.R.H., A.P. and F.B. performed all NMR experiments and analysed the data. S.M. collected the HRMS data and analysed them with F.B. The electrical conductivity measurements were performed by B.K.S. and A.D. The electrical conductivity data were analysed by B.K.S. and S.K.S. The X-ray total scattering data were collected by T.D.B., A.F.S., M.F.T., L.N.M., D.A.K., D.S.K. and P.A.C. The total scattering data were analysed by B.K.S., D.A.K., A.F.S. and T.D.B. Interpretation and analysis of molecular simulations were performed by M.D. and F.-X.C. who also analysed the data. B.K.S. collected and analysed all other data. All authors participated in manuscript writing, led by T.D.B. and B.K.S.

Competing interests

The authors declare no competing interests.

Additional information

Supplementary information The online version contains supplementary material available at https://doi.org/10.1038/s41557-021-00681-7.

Correspondence and requests for materials should be addressed to T.D.B.

Peer review information *Nature Chemistry* thanks Maria Senaris-Rodriguez and the other, anonymous, reviewer(s) for their contribution to the peer review of this work.

Reprints and permissions information is available at www.nature.com/reprints.